Complete angular distribution measurements of pp spin correlation parameters A_{xx}, A_{yy}, and A_{xz} and analyzing power A_y at 197.4 MeV

F. Rathmann,[1,*] B. von Przewoski,[2] W. A. Dezarn,[2,†] J. Doskow,[2] M. Dzemidzic,[2] W. Haeberli,[1] J. G. Hardie,[2,‡] B. Lorentz,[1] H. O. Meyer,[3] P. V. Pancella,[4] R. E. Pollock,[3] T. Rinckel,[2] F. Sperisen,[2] and T. Wise[1]

[1]*Department of Physics, University of Wisconsin-Madison, Madison, Wisconsin 53706*

[2]*Indiana University Cyclotron Facility, Bloomington, Indiana 47405*

[3]*Department of Physics, Indiana University, Bloomington, Indiana 47405*

[4]*Western Michigan University, Kalamazoo, Michigan 49008*

(Received 2 March 1998)

Measurements of pp spin correlation coefficients A_{xx}, A_{yy}, and A_{xz} and analyzing power A_y for pp elastic scattering at 197.4 MeV over the laboratory angular range 3.5°–43.5° ($\theta_{\text{c.m.}}=7°-90°$) have been carried out. The typical statistical accuracy per 1° angle bin is better than 0.02 for the A_{mn} and better than 0.005 for A_y. Systematic errors are negligible except for an overall normalization uncertainty of 2.5% for A_{mn} and 1.3% for A_y. The experiment makes use of a polarized hydrogen gas target internal to a proton storage ring (IUCF Cooler) and a circulating beam of polarized protons. The target polarization is switched in sign and direction (x, y, z) every 2 s by reversing a weak guide field ($\approx$0.3 mT). Scattered and recoil protons are detected in coincidence by two sets of wire chambers, by scintillators, and by silicon-strip recoil detectors placed 5 cm from the proton beam. Analysis methods and comparison to recent pp partial-wave analyses and NN potential models are described. [S0556-2813(98)05008-0]

PACS number(s): 13.88.+e, 24.70.+s, 13.75.Cs, 25.40.Cm

I. INTRODUCTION

In a recent paper [1], we reported measurements of spin correlation parameters in pp elastic scattering near 200 MeV for laboratory angles forward of 17.5°. In the past, measurements involving polarized beams and polarized targets were rather difficult, because solid polarized H targets contain a large fraction of material other than hydrogen, and the targets are subject to deterioration by radiation damage. However, experience with the recent experiment [1] showed that results of high statistical accuracy and small systematic errors can be obtained by a new technique, which involves the interaction of a polarized proton beam stored in a ring with a thin internal gas target of polarized H atoms. In view of the success of the earlier experiment, the apparatus was modified to permit measurements of pp spin correlation parameters over the full angular range. This paper reports values of the analyzing power A_y and spin correlation parameters A_{xx}, A_{yy}, and A_{xz} at 197.4 MeV as a function of angle for the laboratory angular range 3.5° to 43.5° ($\theta_{\text{c.m.}}=7°$ to 90°).

In many respects, the experimental methods developed in connection with the earlier measurements still apply and thus will not be covered here in detail. Section II presents a brief overview and describes the changes in the experimental setup that were required to extend the accessible range of scattering angles. The method of data acquisition differed significantly from the earlier work: measurements at $T_0=197.4$ MeV were combined with data acquisition at seven higher energies between 250 MeV and 450 MeV. The idea was to accelerate and later decelerate the stored beam and to take measurements at T_0 before acceleration and after deceleration as described in Sec. III. In this way it was possible to relate the absolute calibration of beam and target polarization at the higher energies to the calibration at T_0 reported in Ref. [1]. The results at higher energies will be described in a separate paper. For the present purposes the acceleration to higher energies presents a minor complication in that the beam polarization may have been different for data taken before and after deceleration. Besides the data taking procedure, Sec. III also reviews the data processing and the selection of valid pp events, while Secs. IV and V summarize results related to luminosity and beam and target polarizations.

Measurements are taken with transverse (vertical) beam polarization $\pm P_y$ and with target polarization changing between $\pm Q_x$, $\pm Q_y$, and $\pm Q_z$. The resulting 12 yields for each angle bin are analyzed to determine the analyzing power and the three spin correlation parameters (Sec. VI). Corrections and systematic errors are summarized in Secs. VII and VIII, respectively. The final results are reported in Sec. IX and compared to the earlier results over the more limited range of angles. Comparisons to various phase shift solutions and pp potential models are presented in Sec. X.

II. EXPERIMENTAL ARRANGEMENT

A. Overview

A simplified top view of the target and the detector system is shown in Fig. 1. The polarized proton beam circulat-

*Present address: Physikalisches Institut der Universität Erlangen-Nürnberg, 91058 Erlangen, Germany; working at Forschungszentrum Jülich GmbH, 52425 Jülich, Germany.

†Present address: Wake Forest University School of Medicine, Winston-Salem, NC 27157.

‡Present address: Christopher Newport University, Newport News, VA 23601.

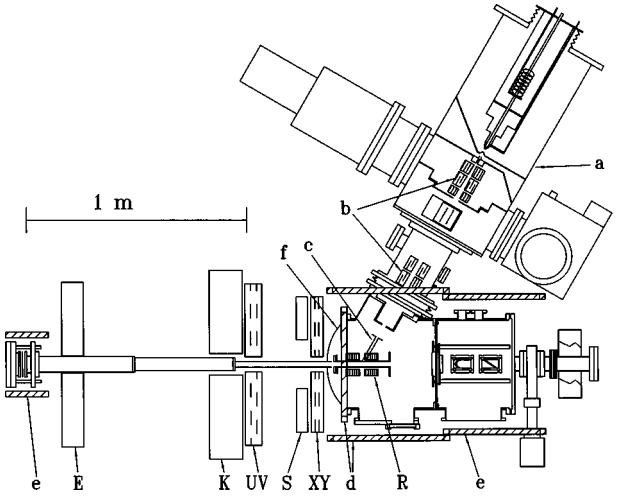

FIG. 1. Top view of the experimental setup. In the atomic beam source (a), hydrogen hyperfine states $|1\rangle=|m_j=+\frac{1}{2},m_I=+\frac{1}{2}\rangle$ and $|2\rangle=|+\frac{1}{2},-\frac{1}{2}\rangle$ are selected according to their electron spin in a segmented system of sextupole magnets (b). After passage through a medium field rf transition the atoms are injected into the feed tube (c) of the storage cell. The target polarization can be chosen along $\pm x$, $\pm y$, and $\pm z$ by field coils (d) (see Fig. 2 for coordinate system). The coils for $\vec{B}\|y$ are not shown. Two compensation coils (e) reduce vertical closed orbit distortions of the stored proton beam. Scattered protons pass through a spherical exit window (f) and are detected by a system of scintillation counters (E, K, S) and wire chambers (XY and UV), while silicon-strip detectors (R) near the storage cell respond to recoil protons.

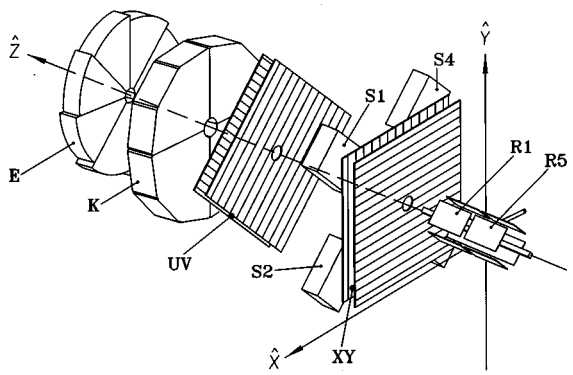

FIG. 2. Three dimensional representation of the detector setup used to record pp elastic scattering events between $\theta_{\rm lab}=3.5°$ and 60°. Eight silicon microstrip detectors R1 through R8 are located alongside the target cell. The beam momentum is along the $+z$ direction. The forward detector array consists of two wire chambers, XY and UV, and two planes of multisegmented scintillation counters, K and E. Four scintillation counters S1 through S4 are located behind the first wire chamber at azimuthal angles of $\pm 45°$ and $\pm 135°$, covering scattering angles $30°-60°$. Events are triggered in two ways: type I events are coincidences between any of the eight recoil detectors R1 through R8 and a scintillator signal in either the K or the E scintillation counters. At larger angles elastic pp events of type II are triggered through two proton coincidences between any of the two scintillation counters above the beam axis, S1 and S4, and any of the two below the beam axis, S2 and S3.

ing in the IUCF ''Cooler'' [2] passes through the target, which is mounted in a low-dispersion straight section [section (a)]. Polarized atoms from an atomic-beam source are injected into a T-shaped storage cell with thin Teflon walls. The direction of target polarization is horizontal, vertical, and longitudinal, depending on the direction of a magnetic guide field provided by an array of Helmholtz coils. Elastically scattered protons are detected in coincidence by a system consisting of scintillators, wire chambers, and silicon strip detectors (Fig. 2). Below we primarily describe those parts of the equipment that differ from the earlier experiment [1]. For a description of trigger conditions and identification of pp events, see Sec. III.

B. Target

An atomic beam source, which is described in Ref. [3], produces a beam of polarized H atoms in a single hyperfine state (state 1, $m_I=\frac{1}{2}$, $m_j=\frac{1}{2}$, see Ref. [4]) for which the nuclear polarization with respect to the external guide field is, ideally, $P=1$ independent of the strength of the external magnetic field. Spin state selection is accomplished by placing a suitable rf transition unit between two spin separating sixpole magnets [(b) in Fig. 1]. About 3.5×10^{16} polarized H/s are injected into the entrance tube of a T-shaped target cell, the purpose of which is to enhance the target thickness compared to that of the atomic beam itself by about a factor of 100. The target cell differs from that used in the earlier experiment [1] in that the 25.4 cm long channel through which the beam passes has a square aperture of 10 mm $\times$ 10 mm, compared to the 8 mm $\times$ 8 mm aperture used previously. For the present experiment, which required frequent changes in the energy of the stored beam, the larger acceptance of the cell was advantageous because it provided more flexibility in tuning the ring. Enlarging the aperture from 8 mm to 10 mm increased the gas conductance out of the cell and thus reduced the target thickness from 3×10^{13} H/cm^2 to 2×10^{13} H/cm^2. Part of the loss in target thickness is offset by the increase in beam current [5]. As before, the cell wall was made of 0.43 mg/cm^2 Teflon foil. The energy loss of scattered protons in the foil is less than 100 keV.

The target guide field of about 0.3 mT is provided by coils external to the target vacuum chamber. Details of the guide field configuration and the compensation coils which are used to reduce the effects of the guide field on the proton closed orbit are described in Ref. [1]. The direction of the target polarization is switched every 2 s between $\pm x$, $\pm y$, and $\pm z$ (see Fig. 2 for coordinate system).

C. Detector configuration, trigger, and event types

Forward scattered protons exit the scattering chamber through a spherical window of uniform thickness (0.34 mm) spun from a sheet of stainless steel [(f) in Fig. 1]. The foil is supported by radial struts positioned at azimuthal angles outside the ϕ acceptance of the detectors. The window allows unobstructed passage of protons between 6° and 60° in the laboratory. The rms multiple scattering angle for protons near 45° is 0.75°.

The forward scintillators (E and/or K) respond to pp scattering in the angular range 3° to 35°. The small angle cutoff is given by the inner hole of the E detector while the outer boundary of the K detector defines the large angle cutoff. Coincidences triggered by either forward scintillator and any

of the eight silicon strip recoil detectors will be labeled *type I* events. The laboratory scattering angle of the forward proton is normally determined from the coordinates in the XY and UV wire chambers (angular range $8° < \theta_{lab} < 35°$) or only the UV chamber ($5° < \theta_{lab} < 8°$). However, for the smallest scattering angles ($\theta_{lab} = 3°$ to $5°$) the forward proton passes through the center hole of both wire chambers and the scattering angle is determined from the energy of the recoil proton (see Sec. III C 2). Type I events for which the scattering angle is determined by the wire chambers are referred to as *type Ia* events, while events whose scattering angle is determined from the pulse height in the silicon recoil detector are referred to as *type Ib*.

Scattered protons in the angular range $30° < \theta_{lab} < 60°$ were detected by scintillators S1 through S4 (25 cm $\times$ 25 cm $\times$ 5 cm thick) placed immediately behind the first wire chamber at azimuthal angles $\pm 45°$ and $\pm 135°$ (Fig. 2). The azimuthal acceptance (about $\pm 40°$) safely overlaps the ϕ acceptance of the recoil detectors. *Type II* events were triggered by a coincidence of two of these scintillators, one above the beam axis (S1 or S4) and one below the beam axis (S2 or S3).

1. Recoil detectors

Eight 1 mm thick silicon-strip recoil detectors are placed 50 mm from the beam axis as shown in Fig. 2. As was the case in the earlier experiment, the detectors are centered at azimuthal angles of $\pm 45°$ and $\pm 135°$. The active area of each detector is 39 mm $\times$ 61 mm, where the long dimension is along the beam direction (see Fig. 2 of Ref. [1]). The corresponding ϕ acceptance is about $\pm 22°$. Each detector has 28 strips spaced 2.19 mm from one another. In order to achieve more complete depletion and better energy resolution than was available in the earlier experiment, the new detectors purchased for the present experiment [6] use a separate guard ring, which permits higher applied voltage without excessive noise from breakdown. The detectors were cooled to about 0 °C.

2. Forward scintillators

The segmented E detector was previously used for other experiments [7,1]. In order to increase the angular acceptance and energy resolution of the forward detector, a second scintillator (K in Fig. 2) consisting of four 15 cm thick segments was added. Each segment is read out by three phototubes. The K scintillator has inner and outer diameters of 10 cm and 85 cm, respectively. This detector was built primarily in preparation of later work on π^0 production. In the present experiment, information on energy deposited in the E and K detectors was not used.

3. Wire chamber

For large-angle events (type II triggers), event reconstruction is based on the coordinates of both proton tracks in the first wire chamber. A new wire chamber (XY in Fig. 2) was built to improve the accuracy of the position information. To accommodate the beam pipe, the wires are supported from a hub structure much like the second chamber, which is described in Ref. [8]. The new wire chamber has a wire spacing of 3.2 mm and an inner diameter of the hub of 2.9 cm, compared to 6.4 mm and 7.6 cm, respectively for the second chamber. The reduced wire spacing of course also improves the accuracy of the track reconstruction for type Ia events.

III. DATA ACQUISITION, PROCESSING, AND SELECTION OF EVENTS

A. Measuring cycle

The measurements were carried out in cycles, each consisting of four parts: (i) 3 min beam injection of vertically polarized beam of energy $T_0 = 197.4$ MeV; (ii) 0.8 min data acquisition at T_0; (iii) 4 min data acquisition at energies between 250 MeV and 450 MeV; (iv) 1.2 min data acquisition at T_0.

The beam was injected from the cyclotron, which is equipped with a polarized-ion source. Beam accumulation in the Cooler made use of multiturn injection and stacking in the presence of electron cooling. Between parts (ii) and (iii) of the cycle, the stored beam was accelerated by upramping the ring, while between parts (iii) and (iv) the stored beam was downramped back to the initial energy T_0.

Data acquisition was organized in subcycles of 12 s duration, during which the target polarization was switched every 2 s in the directions $\pm x$, $\pm y$, $\pm z$. Part (ii) of the cycle, consisting of 4 subcycles, will be referred to as the ''PRE'' part of the measuring cycle. Part (iv), consisting of 6 subcycles, will be referred to as the ''POST'' part of the cycle. At least 96% of the initial beam polarization survived the two ramps in a cycle. The small difference in PRE and POST beam polarization has no effect on the present measurements since the pp measurement itself provides a continuous monitor of beam polarization.

At the end of a completed cycle, the polarization of the stored beam is reversed by exposing the beam to an adiabatic transition through an artificially introduced spin resonance. The operation of this ''spin-flipper'' is described in Ref. [9]. For the following cycle, beam of opposite polarization is accumulated to add to the spin-flipped remainder of the beam from previous cycles. The average luminosity is thereby enhanced by about a factor four compared to discarding the beam at the end of each cycle [10]. Reversal of the polarization direction of the injected beam was accomplished by switching rf transitions at the ion source.

B. Recorded data

The trigger conditions and event types are described in Sec. II C. The event record includes the pulse heights of all scintillators and recoil detectors and the time with respect to the occurrence of the trigger. The record also specifies which of the silicon strips and which of the 448 wires of the four wire planes fired. Also recorded is the time of occurrence of the trigger with respect to the beginning of a cycle and with respect to the current subcycle of the target polarization. Logic levels indicating the sign of the target polarization and the sign of the beam polarization are read out as well. For both types of events the number of triggers offered and the number of triggers processed is read every second. This information is used to determine the deadtime of the data acquisition system.

C. Identification and selection of *pp* events

1. $\theta_{lab}=5°-35°$ (type Ia events)

This angular range is characterized by event records that contain information about the forward proton from one or both pairs of wire planes and information about the recoil proton from the silicon strip detectors. Events of this type were subjected to a kinematic fit to determine best values of scattering angle, azimuthal angle, and the z component of the vertex position, assuming the event originates on the beam axis and follows kinematics of pp elastic scattering. Input to the fit are up to five pieces of information: four positions in the wire chamber planes and one position of the hit in the recoil detector. Because of missing wire chamber information for some events (in particular below $\theta_{\rm lab}=8°$, for which only the second chamber intercepts the track) the number of degrees of freedom ν varies between 0 and 2. To compare events with different degrees of freedom, a fixed value of the integral over the tail of the probability density function, $P(\chi^2,\nu)$, was used [i.e., a fixed ''confidence level'' C.L.; see Eq. (27.24) of Ref. [11]], where $P(\chi^2,\nu)=1-\text{C.L.}(\chi^2,\nu)$. All events with $\nu=0$ (3% of all events) were included in the analysis.

As uncertainty for the hit position in the XY and UV wire chambers we used ± 1 mm and ± 2 mm, respectively. The wire chamber resolution is better than half the wire spacing, because tracks in some region between two wires always fire both of them. The uncertainty of the position in the recoil detectors is ± 1 mm when a single strip responds (86% of all events) and ± 1.5 mm (13%) when two adjacent strips responded. In a case that the position within the recoil detector was ambiguous, and only the detector number is known, an uncertainty of ± 25 mm (1%) is assigned. Events of type I are accepted if the calculated statistical probability $P(\chi^2,\nu)<0.8$. This cutoff corresponds to a χ^2 of 1.64 in the case of $\nu=1$, 3.20 in the case of $\nu=2$, and 4.64 for $\nu=3$. If $P<0.9$ had been chosen instead, the final results would have changed by less than a third of the statistical error.

Events with extraneous hits in the wire chambers and recoil detectors, caused by accidental tracks, are also considered. We included in the analysis events with up to three valid positions in each of the wire chamber planes, as well as the recoil detector. For every possible combination a kinematic fit is performed. Eventually those events are accepted that have the smallest χ^2 and feature forward and recoil protons in opposite quadrants. In this process only events with equal degrees of freedom are compared.

In order to avoid sensitivity to the boundaries of the recoil detectors in the azimuthal direction, events are accepted only within $\pm 18.5°$ around the nominal recoil detector positions. The software cut in ϕ is illustrated in Fig. 3, which shows the hit pattern of events in the second wire chamber.

The kinematic fit does not test for the correlation between scattering angle and recoil energy that is required by a pp event. Figure 4 shows the measured energy deposited in the recoil detector vs the forward scattering angle determined by the kinematic fit. For small angles the recoil energy increases with forward angle, but beyond about 14° the recoils are no longer stopped and the energy deposited in the detector decreases as the scattering angle increases further. Events are accepted within the boundaries of the two-dimensional gate shown in Fig. 4. A gate either twice or half as large in area affects the final results by less than a third of an error bar.

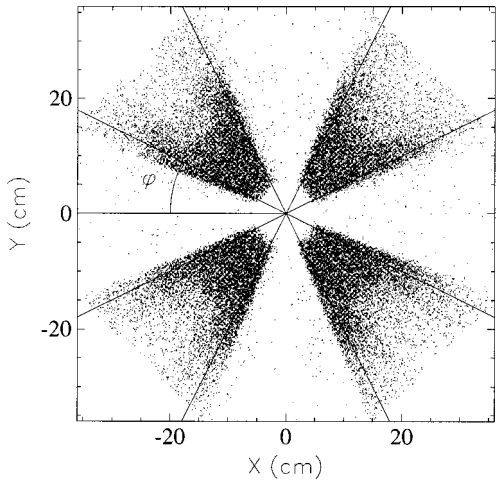

FIG. 3. Pattern of hits in the second wire chamber for events of type I as seen along the beam direction. The acceptance is determined by the azimuthal position of the recoil detectors, nominally centered at $\phi=\pm 45°$ and $\phi=\pm 135°$. The solid lines indicate the boundaries of the azimuthal cut for the final selection of events.

2. $\theta_{lab}<5°$ (type Ib events)

For the smallest angles, where no wire chamber information was available, the scattering angle had to be determined from the energy of the stopped recoil. An absolute energy calibration of the recoil detectors was provided by 5.479 MeV α particles from eight ^{241}Am sources permanently installed on the support structure of the silicon detectors. Figure 5 shows a pulse height spectrum of the 10/s α particles recorded while the proton beam was circulating through the storage cell. The peak position was checked frequently

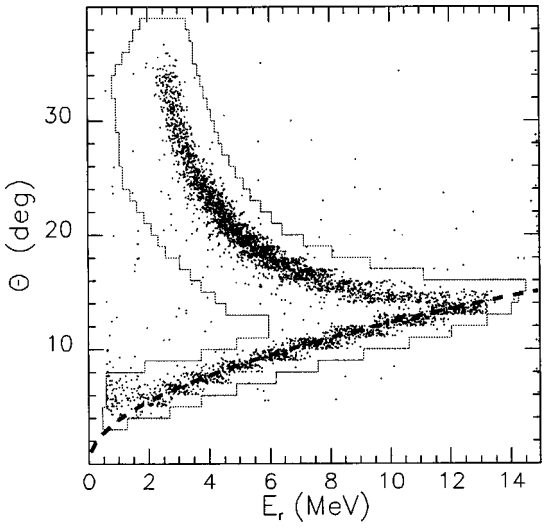

FIG. 4. Energy deposited in the recoil detector vs the forward scattering angle determined by the kinematic fit. Up to a scattering angle of about 13°, recoil protons are stopped in the recoil detectors. Above that angle the pp elastic locus bends over. Events are accepted within the boundaries of the two dimensional gate shown. The dashed line indicates the resulting forward scattering angles calculated from the energy deposited in the recoil detectors alone.

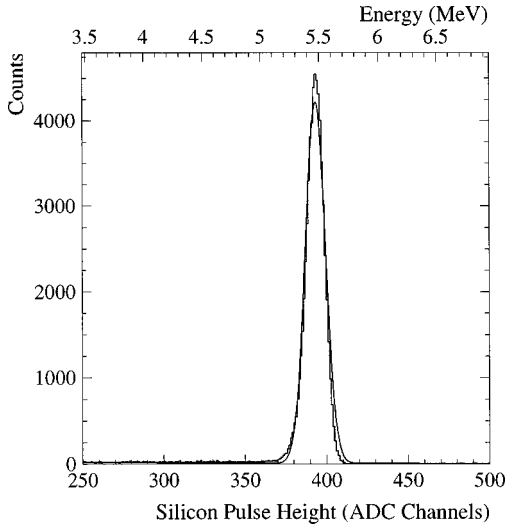

FIG. 5. Pulse height spectrum of a silicon strip recoil detector in the presence of a proton beam through the polarized H target. The peak is caused by α particles from a 10/s ^{241}Am source permanently mounted near the detector. The counts away from the α peak are from *pp* scattering and background. The spectrum illustrates the low singles rate in a detector near the circulating beam. The curve is a Gaussian of width 75 keV.

throughout the measurement and was found to be constant to 0.15%. In Fig. 4, the forward scattering angle calculated from the recoil detector pulse height is shown as a heavy dashed line, showing good agreement with the angle determined from the kinematic fit. The calculated curve takes into account the small energy loss (less than 100 keV at $\theta_{\rm lab} = 3°$) of the recoil protons in the wall of the target cell.

3. θ_{lab}=30°–60° (type II events)

Events of this type are subject to a kinematic fit very similar to the procedure used for type I events. Here up to six pieces of information are available, two positions in the recoil detectors and four positions in the XY wire chamber, since both proton tracks are detected. Events are only accepted for the number of degrees of freedom $\nu \geqslant 1$. A probability cut $P(\chi^2, \nu) < 0.8$ is used. Events are only accepted if the azimuthal angle returned from the kinematic fit falls within the $\pm 18.5°$ boundaries indicated in the hit pattern of events in Fig. 6.

D. Compensation for detector misalignment

The target cell and the various detectors were aligned with respect to the nominal alignment axis of the Cooler straight section by standard surveying methods. However, data analysis is much simplified if the *z* axis (Fig. 2) is taken to be the effective center of the proton beam. Thus software corrections are made to the detector position to take into account that the proton beam does not exactly coincide with the nominal alignment axis, and to allow for changes of proton beam position with time. The proton beam position changes by about 2 mm over a period of a week, but it also changes a similar amount between the PRE and POST part of a given cycle. For every few hours of recorded data the

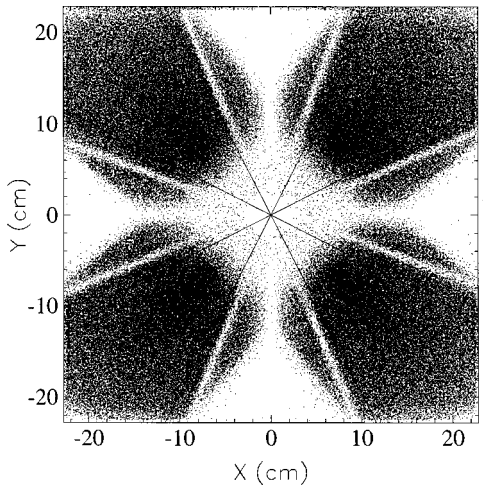

FIG. 6. Pattern of hits in the first wire chamber for events of type II. As in Fig. 3, the solid lines indicate the boundaries of the azimuthal cut for the final selection of events. The shadows of the spokes which support the exit window are clearly visible. The four lobes correspond to the scintillators S1–S4 in Fig. 2.

detector position is adjusted in software to correspond to the actual beam axis, making use of the observed *pp* events themselves.

There is also a small effect of the guide field on the position and angle tilt of the beam. In the preceding experiment it was shown that neither position nor angle tilt fluctuations induced by reversal of the direction of the guide field cause any effect on the final data [1]. Therefore these effects are neglected in the analysis of the data presented here.

1. Longitudinal position of the wire chambers

As long as the recoil proton stops in the silicon detector, the scattering angle for each event can be determined from the known recoil energy (see Sec. III C 2). The laboratory angle of the corresponding forward track, determined from the kinematic fit, will be inconsistent with the recoil energy if the longitudinal position (z) of the wire chamber is incorrect. The longitudinal position of both wire chambers is adjusted so as to obtain best agreement between the two methods. The method is insensitive to a transverse displacement of the wire chambers because events for all azimuthal angles are averaged. The longitudinal position uncertainty for the first and second wire chamber is ± 0.5 mm and ± 0.8 mm respectively. The corresponding uncertainty in scattering angle is $\leqslant 0.08°$.

2. Transverse position of the wire chambers and recoil detectors with respect to beam

For type II events, scattered and recoil protons are both recorded in the first wire chamber (XY chamber). A straight line that connects the two hits in the XY chamber must pass through the beam axis, since *pp* events are coplanar. A subsequent event at different ϕ establishes a second straight line whose intercept with the first yields a beam position in the XY plane. Repeating the process for a large number of events yields the hit pattern of intercepts shown in Fig. 7. The pattern does not reflect the beam diameter because it is smeared out by finite wire chamber resolution. For Fig. 7, the

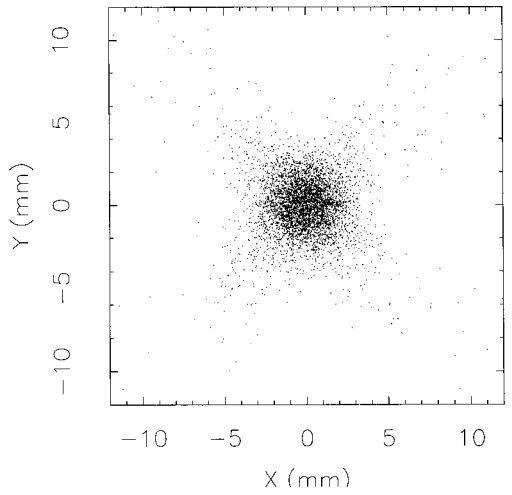

FIG. 7. Crossing of straight lines connecting the two hits in the XY chamber for subsequent events allow to precisely center the first wire chamber onto the proton beam axis. The centroid of the distribution once projected onto the x and y axis, respectively, allows us to determine x and y corrections to the transverse wire chamber position with a precision better than 0.05 mm.

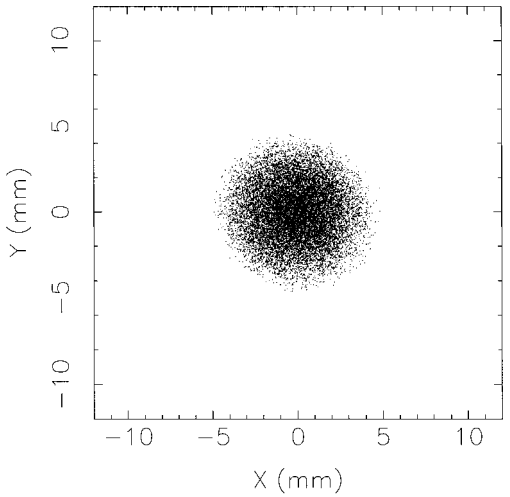

FIG. 9. Overlay of straight line intercepts of the hits in the first and second wire chamber with a plane perpendicular to the beam at the individual vertex determined from the kinematic fit for type Ia events. A correction to the transverse position of the second wire chamber was applied to center the hit pattern on the coordinate frame.

x and y position of the first wire chamber is already corrected in software such that the centroid of the hit pattern coincides with the center of the coordinate frame in which the data are analyzed.

The above method was used to monitor changes in beam position over time during the measurements. In Fig. 8 the beam walk over a two week period is shown for the PRE and POST phases of the measuring cycle. The statistical accuracy of the method (± 0.02 mm) is surprisingly high. After the downramp, the beam is about 1 mm to the right of the original position.

For the second wire chamber, transverse offsets were determined from type Ia events, for which the forward track produces hits in all four wire chamber planes. The kinematic fit of forward track and z position of the recoil detector strip that fired determines a vertex position for each event. A straight line through the original hits in the wire chambers intercepts a plane perpendicular to the beam direction at the vertex position. An example of an $x-y$ distribution of intercepts is shown in Fig. 9. The position of the pattern was adjusted to be at the origin by applying a suitable transverse correction to the second wire chamber position, while the first wire chamber remained unchanged.

The spacing between opposite recoil detectors was determined with an accuracy of ± 1 mm from a photograph of the cell-detector assembly, taken along the cell axis prior to installation. For a large fraction of type II events vertices can be obtained separately for each of the two forward tracks from scattering and azimuthal angles. Any mismatch between the two vertices leads to a transverse position correction of each pair of recoil detectors where the distance between the detectors stays the same.

All the above adjustments were repeated a number of times in an iterative fashion since they are slightly interdependent.

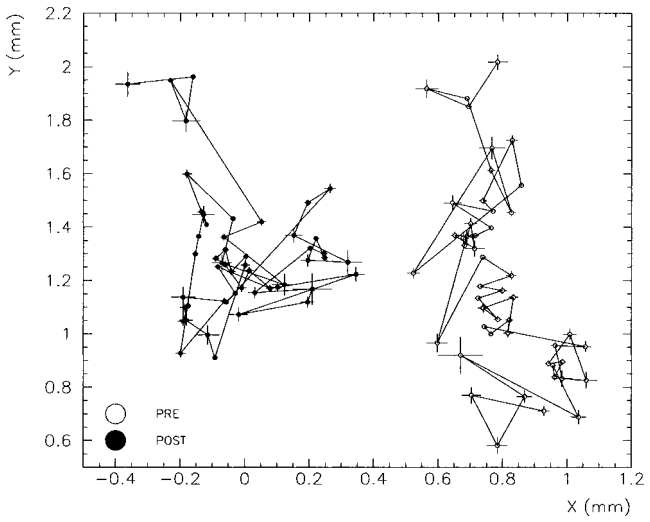

FIG. 8. Beam position changes during two weeks of data taking for the PRE (○) and POST (●) part of the measuring cycle. The beam position was determined from a hit pattern similar to Fig. 7.

IV. BEAM CURRENT, LUMINOSITY, AND EVENT RATE

Accumulation rates of beam in the ring during injection were typically in the range 10–30 μA/min. After beam had accumulated for several cycles, the stored beam intensity was 100–400 μA during data acquisition. The trigger rate is about 1.3 s^{-1} μA^{-1}, of which typically 30% are good events.

Compared to the previous experiment [1], the target thickness available here was lower by a factor 1.5 because of the increased cell aperture. The detectors view about 70% of the total target thickness of $d_t = 2 \times 10^{13}$ H/cm^2. Under best conditions, a luminosity of 4.5×10^{28} s^{-1} cm^{-2} was achieved.

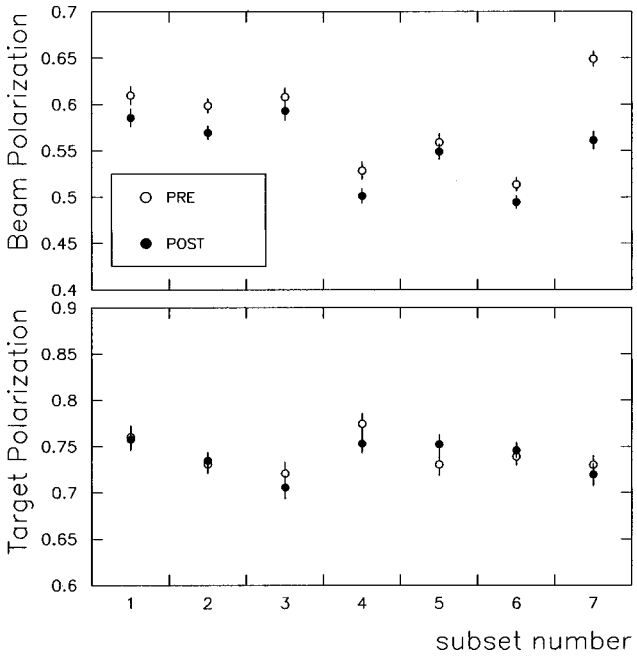

FIG. 10. The top panel shows the beam polarization P_y during two weeks of data taking for the two parts PRE and POST of the measuring cycle. Each subset corresponds to one particular beam energy after the upramp. In the lower panel the corresponding values of the weighted average $\langle Q_x, Q_y \rangle$ are shown.

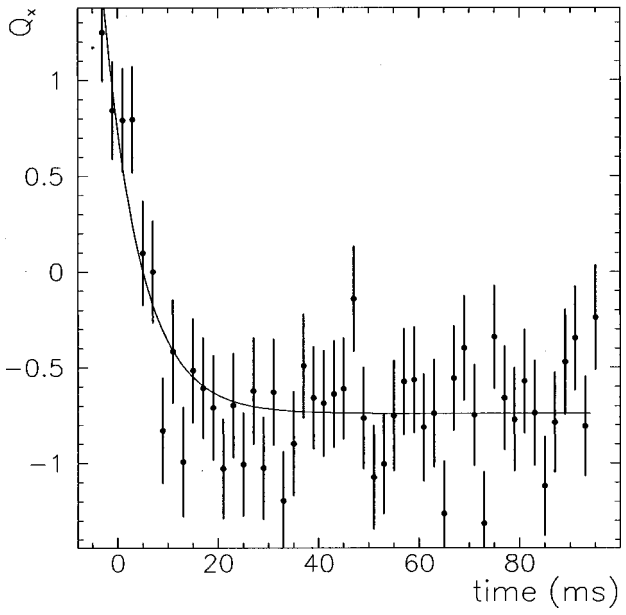

FIG. 11. Reversal of the target polarization as a function of time in a subcycle. The exponential fit corresponds to a lifetime of $\tau = 7 \pm 1$ ms.

V. BEAM AND TARGET POLARIZATION

The determination of beam and target polarization is based on the measured count rate asymmetries and the known pp analyzing power and spin correlation coefficients reported in Ref. [1]. The normalization procedure is described in Sec. VI B. Figure 10 shows target and beam polarization during two weeks of data taking. Data before and after ramping to the higher energy are shown separately. The data were grouped into seven sets, corresponding to the seven energies to which the beam was ramped. The figure illustrates that the postramp beam polarization is consistently lower than the preramp polarization by about 4% (see also Ref. [12]) except for one data set (ramping to 450 MeV) when the difference was 14%. The changes in beam polarization have no adverse effect on the final data, since data taken before and after the ramp were analyzed separately using the appropriate polarization values.

The target polarization Q_x and Q_y with guide fields in x and y directions, respectively, are the same within statistics. In Fig. 10, the values of the target polarization are averages of Q_x and Q_y.

The experiment yields also detailed information about components of beam and target polarization perpendicular to the desired components. Table I lists for each of the three target guide fields the wanted components (in boldface) as well as the corresponding unwanted components that reverse with reversal of the guide field. The lack of exact reversal of the target polarization is taken into account by adding to the exactly reversing guide field the nonflipping components S (Table I). The purpose of Table I is to show that the deviations from the ideal guide field configuration are small. Although the effects of these unwanted components on the final results are negligible, the extraction of the analyzing powers and spin correlation parameters took them into account.

One advantage of hydrogen gas targets over solid targets is that they afford rapid change in the target polarization. The reversal of the target polarization Q from $+Q_x$ to $-Q_x$ is shown in Fig. 11. The curve is an exponential fit to the data with a time constant $\tau = 7 \pm 1$ ms. After 35 ms the polarization differs from its asymptotic value by less than 1%. The rise time is given by the time constant of the magnet power supply rather than the dwell time of the atoms in the cell (3 ms). It should be noted that the finite polarization reversal time has no effect on the final data, because only the average target polarization enters in the analysis. Nevertheless, after reversal of the target polarization a delay of 100 ms was introduced before resuming data acquisition.

VI. DETERMINATION OF SPIN CORRELATION COEFFICIENTS

A. Relation between yields and spin-correlation coefficients

For pp elastic scattering, the spin-dependent cross section for polarized beam and polarized target in units of the unpolarized cross section is given by[1]

[1]Equation (1) of Ref. [1] contained an error in the term containing $(p_x q_x + p_y q_y)$. For the particular values of ϕ that were used the error had no effect on the analysis. In Appendix A of Ref. [13] and the SAID database [14], $C_{zx} = -C_{xz}$ should be replaced by $C_{zx} = C_{xz}$, and correspondingly the sign of $p_z q_y$ and of $p_z q_x$ in Eq. (A3) should be reversed. Definitions of the analyzing power A_y and the spin correlation parameters A_{mn} in terms of the nucleon-nucleon scattering matrix M are given, e.g., in Eqs. (5.31) and (6.3) of Ref. [15].

$$X=\sigma/\sigma_0=1+A_y[(P_y+Q_y)\cos\phi-(P_x+Q_x)\sin\phi]+A_{xx}[P_xQ_x\cos^2\phi+P_yQ_y\sin^2\phi$$
$$+(P_xQ_y+P_yQ_x)\sin\phi\cos\phi]+A_{yy}[P_xQ_x\sin^2\phi+P_yQ_y\cos^2\phi-(P_xQ_y+P_yQ_x)\sin\phi\cos\phi]$$
$$+A_{xz}[(P_xQ_z+P_zQ_x)\cos\phi+(P_yQ_z+P_zQ_y)\sin\phi]+A_{zz}P_zQ_z, \quad (6.1)$$

where the polarization components $P_{x,y,z}$ and $Q_{x,y,z}$ of beam and target, respectively, refer to the coordinate system shown in Fig. 2 [15,16]. The azimuthal angle ϕ is defined in Fig. 3. The analyzing power A_y and the spin correlation coefficients A_{mn} are functions of the scattering angle θ. Since beam and target are identical, no distinction needs to be made between beam and target analyzing power. In the present case to a very good approximation $P_x=P_z=0$, so that Eq. (6.1) simplifies to

$$X=1+A_y[(P_y+Q_y)\cos\phi-Q_x\sin\phi]$$
$$+A_{xx}[P_yQ_y\sin^2\phi+P_yQ_x\sin\phi\cos\phi]$$
$$+A_{yy}[P_yQ_y\cos^2\phi-P_yQ_x\sin\phi\cos\phi]$$
$$+A_{xz}P_yQ_z\sin\phi. \quad (6.2)$$

For each particular orientation of the target guide field (x,y,z), yields $Y_{ik}(\theta)$ were measured as a function of scattering angle at four azimuthal angles ϕ_i $(i=1,\ldots,4)$ for four different combinations k of the sign of beam and target polarization $(++, +-, -+, --)$. Thus for each orientation of the target guide field, the yield Y_{ik} (number of counts in a given angle bin) is represented by a 4×4 matrix. These yields are related to X [Eq. (6.1)] by factors which contain detector efficiencies ϵ_i on one hand and luminosities λ_k (target thickness, number of incident protons) for the different combinations k of beam and target spin on the other hand. Multiplication of the rows i of Y_{ik} by suitable efficiency factors compensate for differences in detector efficiencies, while multiplication of the columns k by luminosity factors normalizes the luminosity such that for an unpolarized beam and target $X_{ik}=1$.

In principle, the row and column factors could be determined by repeating the experiment with unpolarized beam and target, and normalizing the yields based on accurately measured target thicknesses and integrated beam currents. However, since combinations of yields for different beam and target polarization states can be combined to produce in effect an unpolarized target and/or an unpolarized beam, it is plausible that the Y_{ik} themselves can be used to determine the appropriate efficiencies and luminosities.

The procedure by which the X_{ik} matrix is calculated from the Y_{ik} matrix is referred to as *diagonal scaling*. The method is outlined in Ref. [1], and documented in more detail in Ref. [13]. The transformation from Y_{ik} to X_{ik} is unique. The resulting three matrices X_{ik}, corresponding to the three orientations of target guide field, are used to determine the analyzing power A_y, the spin correlation parameters A_{mn} and the various components of beam and target polarizations (Table I). The yields are binned in 1° lab angle intervals. The beam and target polarization are common to all angle bins, while the efficiency and luminosity scale factors are determined for each angle bin separately.

As pointed out earlier [1], the diagonal scaling method was compared to an alternative method of deducing the observables from a nonlinear least-squares fit, where the ingredients in the theoretical expression for the yields were varied to fit the measured Y_{ik}. The two methods gave identical results.

The above procedures leave undetermined an adjustable scale factor, which describes the absolute polarization calibration. The absolute normalization is described in the following subsection.

B. Absolute normalization of beam and target polarization

The data analysis yields five statistically independent angular distributions of polarization observables:

$$P\cdot A_y(\theta_i),$$
$$Q\cdot A_y(\theta_i),$$
$$P\cdot Q\cdot A_{xx}(\theta_i), \quad (6.3)$$
$$P\cdot Q\cdot A_{yy}(\theta_i),$$
$$P\cdot Q\cdot A_{xz}(\theta_i),$$

where θ_i ranges from 3.5° to 43.5° in 1° angle bins. Determination of the A_y and A_{mn} is straightforward once P and Q are known. Here we address the determination of the absolute values of beam and target polarizations, P and Q. The determination of P and Q was done separately for the measurements before and after ramping to higher energies, and was done separately for each data set corresponding to a particular energy after acceleration.

In order to determine absolute values of the beam and target polarizations, P and Q, we make use of previous absolute measurements of $A_y(\theta)$, $A_{xx}(\theta)$, $A_{yy}(\theta)$, and $A_{xz}(\theta)$. While the earlier results covered the angular range $\theta_{\rm lab}=4.5°$ to 17.5°, here we ignore the data below 8.5° because at the smallest angles the analyzing powers are small and are probably more sensitive to systematic errors. Since the results of Ref. [1] differ by 0.4 MeV in energy from the present results, a small correction was applied to the data of Ref. [1] using theoretical slopes of the observables with respect to energy.

First we note that the ratio of beam and target polarization in the present experiment is determined to very high statistical accuracy because the same analyzing power A_y is measured over the entire range of angles in the same run, once from the beam asymmetry PA_y and once from the target asymmetry QA_y. The ratio $R=P/Q$ was determined as the weighted mean of the ratios $PA_y(\theta_i)/QA_y(\theta_i)$ for the angle

TABLE I. Complete set of Cartesian polarization components of beam and target for the two parts, PRE and POST, of the measuring cycle and the target guide field orientations $\pm x$, $\pm y$, and $\pm z$. The large wanted components of beam and target polarization are shown in boldface. There are unwanted components such as S_{P_y}, S_{Q_x}, and S_{Q_z} that do not flip sign with guide field and those that reverse with guide field in a direction perpendicular to the desired orientation.

	$\pm x$		$\pm y$		$\pm z$	
	PRE	POST	PRE	POST	PRE	POST
P_x	0.0052(47)	0.0089(44)	0.0052(47)	0.0089(44)	0.0052(47)	0.0089(44)
P_y [a]	**0.5801(34)**	**0.5425(32)**	**0.5802(34)**	**0.5417(32)**	**0.5765(34)**	**0.5447(32)**
P_z	−0.0021(47)	0.0003(44)	−0.0021(47)	0.0003(44)	−0.0021(47)	0.0003(44)
Q_x	**0.7401(59)**	**0.7394(56)**	−0.0039(59)	0.0039(56)	−0.0071(23)	−0.0052(23)
Q_y	0.0111(59)	0.0039(56)	**0.7400(59)**	**0.7406(56)**	−0.0055(59)	−0.0034(56)
Q_z	0.0158(60)	0.0240(60)	−0.0174(61)	−0.0121(61)	**0.7401(42)** [b]	**0.7400(40)** [b]
S_{P_y}	−0.0008(18)	−0.0005(17)	−0.0008(18)	0.0005(17)	−0.0008(18)	0.0005(17)
S_{Q_x}	0.0017(23)	−0.0007(23)	−0.0040(23)	−0.0031(23)	−0.0043(23)	−0.0024(23)
S_{Q_z}	−0.0091(82)	−0.0162(82)	−0.0177(82)	−0.0197(82)	0.0013(82)	−0.0086(82)

[a]In the analysis the average of the beam polarization for all three states of the target is used.
[b]For longitudinal guide field $Q_z=\frac{1}{2}(Q_x+Q_y)$ is assumed in the analysis.

bins $\theta_i=18.5°$ to 41.5°. The reason to use only angles above 18.5° is that the determination of R is thus statistically independent of the absolute normalization to the previous data between 8.5° and 17.5°. Because of the large range of angles used in the determination of R, the error in R can be neglected compared to other uncertainties in the normalization.

Replacing Q by P/R in expressions (6.3) yields for each of the 10 angle bins from 8.5° to 17.5 ° two terms containing P and three terms containing P^2. The normalization procedure consists of varying P simultaneously in all 50 terms until the present A_y, A_{mn} agree best with the corresponding data of Ref. [1]. In calculating χ^2, the statistical errors of the present and the previous data were taken into account. The uncertainty in the absolute normalization will be discussed in Sec. VIII C.

VII. CORRECTIONS

A. Deadtime

The deadtime of the data acquisition system depends on the total count rate. Since the rate differs depending on beam and target polarization, deadtime corrections to the yields were evaluated. The fractional deadtime was obtained from a comparison of the number of triggers generated, as counted by a fast scaler, to the number of triggers processed by the data acquisition computer. This information yielded the loss probabilities $p_{i=1\ldots12}$ for each of the 6×2 spin combinations of beam and target polarizations. The final yield was processed once with and once without the corresponding dead time correction factors $1/(1-p_i)$. The effect of the deadtime correction was consistently below 20% of the statistical error, and was neglected.

B. Correction for nonuniform ϕ acceptance

The azimuthal range (ϕ) of the detector consists of four quadrants with center values $\phi_i=(\pm45°,\pm135°)$ and a range in ϕ of $\pm18.5°$ about the center. The limits in ϕ are imposed by a cut during data analysis. Equation (6.1) contains trigonometric functions that are averaged over the ϕ acceptance. Rather than assuming an ideal, uniform ϕ acceptance, the ϕ averages were calculated for the true ϕ acceptance, which can be determined from the measured, spin-averaged ϕ distribution of the processed events. The deviation from the ideal situation can be expressed in terms of the moments of the actual ϕ distribution. We distinguish between moments that are even in the deviation from the center angles ϕ_i (affecting the trigonometric averages), and those that are odd (causing a shift in the effective centroid of the ϕ range). Below we separately describe the effects of even and odd moments.

Even moments: For our choice of ϕ_i, neglecting odd moments, the relation

$$|\langle\sin^2\phi_i\rangle|=|\langle\cos^2\phi_i\rangle|=1/2$$

is exact. The remaining trigonometric averages of $\sin\phi_j$ and $\cos\phi_j$,

$$c_1=\frac{\sum_{j=1}^{N}\sin\phi_j}{N}=\frac{\sum_{j=1}^{N}\cos\phi_j}{N}$$
$$=\frac{1}{2}\cdot\left(\frac{\sum_{j=1}^{N}\sin\phi_j}{N}+\frac{\sum_{j=1}^{N}\cos\phi_j}{N}\right) \tag{7.1}$$

and

$$c_2=\frac{\sum_{j=1}^{N}\sin\phi_j\cdot\cos\phi_j}{N} \tag{7.2}$$

were obtained by accumulating during the event-by-event analysis the expressions Eq. (7.1) and Eq. (7.2) separately for each angle bin in each quadrant, where N is the total yield per θ bin. In the analysis of type Ia and type II events, the same values of the trigonometric averages c_1 and c_2 were used for all quadrants, since the variations from one quadrant

to the next were negligible. For event type Ib, the azimuthal angle of the event was not determined. In this case, c_1 and c_2 were calculated for a uniformly populated ϕ interval around ϕ_i of $\pm 22.6°$ (the measured geometrical acceptance of the silicon detectors).

Odd moments: Deviations from a uniform detector acceptance which are odd in ϕ manifest themselves in a shift of the ϕ centroids away from the ideal values $\langle \phi_i^{\text{ideal}} \rangle = \pm 45°$, and $\pm 135°$. For type Ia and type II events the centroids were again obtained from the data:

$$|\langle \phi_i^{\text{actual}} \rangle| = \frac{\sum_{j=1}^{N} \phi_j}{N}. \tag{7.3}$$

It can be shown that only one class of centroid shifts, $\langle \phi_i^{\text{actual}} \rangle - \langle \phi_i^{\text{ideal}} \rangle$, has an effect on the data, namely ϕ rotation of a pair of detectors in opposite quadrants, combined with rotation of the other pair in the opposite sense. Including effects of even and odd moments in the analysis changed values of A_{mn} by at most 0.01.

As mentioned earlier, the ϕ position of the silicon detectors had been determined from a photograph. The centroids of the geometrical acceptance of the silicon detectors were used to calculate the centroid shifts for type Ib events. No correction was necessary in this case.

C. Finite θ-bin correction

Below we report values of the observables A_y, A_{mn} at the center of 1° angle bins. A correction arises because the values at the bin center differ slightly from the measured mean over the bin.

In order to calculate a correction, it was assumed that the shape of the angular dependence of the observables can be taken from theory. Theoretical values of the observables were calculated in 0.1° intervals, and were weighted with the actually observed total yields in the corresponding 0.1° intervals. The correction equals the difference between the mean over the bin and the theoretical value at the bin center. The corrections are sizable only where the angular distributions of observables and total yield show large slopes, i.e., in the smallest and largest angle bins, where the corrections are roughly half the statistical error. However, the correction was applied for all angles.

VIII. SYSTEMATIC ERRORS

A. Background

The storage cell wall is about 10^9 times heavier than the polarized gas stored inside, so that interaction between the beam halo and the cell wall is a potential source of background. That background is not a major problem is evidenced by the low count rate in the silicon detectors (Fig. 5) in the energy range of potential pp events even in the absence of a coincidence requirement. The coincidence requirement imposed by the trigger conditions almost completely eliminates background. However, a small fraction of quasifree pp scattering events in the cell wall are indistinguishable from pp scattering in the target gas.

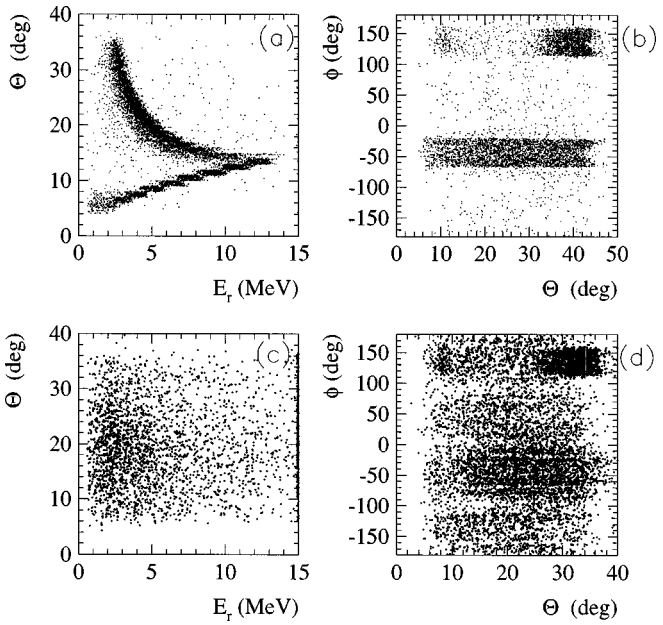

FIG. 12. Comparison of runs with H target [frames (a) and (b)] and N_2 target [frames (c) and (d)]. The frames on the left show the energy, E_r, deposited in the recoil detector vs scattering angle θ of the forward particle determined from the kinematic fit. The frames on the right show the θ vs ϕ determined from the kinematic fit. The events shown are coincidences with one particular recoil detector centered at $\phi = -45°$. The events near $\phi = 145°$, $\theta = 40°$ on frames (b), (d) are true pp coincidences.

During a previous experiment [1] a number of different methods were used to determine the fraction of non-pp events amongst the accepted events. The methods developed there are directly applicable to the present type Ia events, which were obtained under similar conditions. The tightest limits on background were obtained by noting that the forward and recoil particles from background events, such as (p,pX) reactions on C or F in the cell walls, are in general not coplanar. Thus noncoplanar events observed with the H target give an indication how many of the coplanar events, interpreted to be elastic pp events, are caused by background. The top two frames of Fig. 12 show the recoil energy vs forward scattering angle for *one* particular silicon detector centered at $\phi = -45°$ [Fig. 12(a)] and the correlation between scattering angle and ϕ for those same coincident events [Fig. 12(b)]. Events away from the principal loci in these two figures are potential background events.

To determine the relative number of coplanar to noncoplanar events that is characteristic of background, measurements were made with N_2 rather than H in the target, on the assumption that quasifree scattering from N has similar characteristics to scattering from wall material (C and F). Additional discrimination against background for type Ia events is provided by the correlation between recoil pulse height and forward scattering angle required of pp events [Fig. 12(a)]. With the H target, few events are outside the appropriate locus, while for a N_2 target there is no correlation between angle and recoil energy [Fig. 12(c)]. Comparison of ratios of events inside and outside the pp locus between Figs. 12(a), 12(c) on the one hand and Figs. 12(b), 12(d) on the other yields the background fractions given in Table II for type Ia events (for details see Ref. [1]). The results are given sepa-

TABLE II. Background fractions for events of type I and type II of the part before the upramp (PRE) and after the downramp (POST) of the measuring cycle at $T_0 = 197.4$ MeV.

	Type I	Type II
PRE	$(4.9 \pm 0.5) \times 10^{-3}$	$(1.9 \pm 0.2) \times 10^{-3}$
POST	$(5.2 \pm 0.5) \times 10^{-3}$	$(2.4 \pm 0.2) \times 10^{-3}$

rately for the PRE and POST part of the cycle, since the different beam position before and after ramping to higher energies can affect background rates. Background for type Ia events is of the order 0.5% for both parts of the cycle.

For type II events, the coplanarity requirement is very effective in rejecting background, because both protons pass through wire chambers so that the difference in azimuth $\Delta\phi$ is measured accurately. In Fig. 13, $\Delta\phi$ spectra are shown for a polarized H-target run and a short run with N_2 as target. Without tracking, the raw data with the H target show a large narrow peak of pp elastic events riding on top of a broad quasifree peak of background events. The N spectrum (dashed) shows the same broad distribution without elastic peak. The narrow peaks show the events that survive the criteria of the pp kinematic fit (Sec. III C 3). To determine the background fraction, the N spectrum is scaled such that it gives best agreement with the H spectrum on both sides of the elastic peak. The number of accepted pp-like events from N is determined from the scaled spectrum and the background ratio is readily obtained by comparison to the events accepted with the H target. The fraction of background events in the final data is listed in Table II.

From the measured spectra with the nitrogen and the total background fraction it is possible to determine the fractional

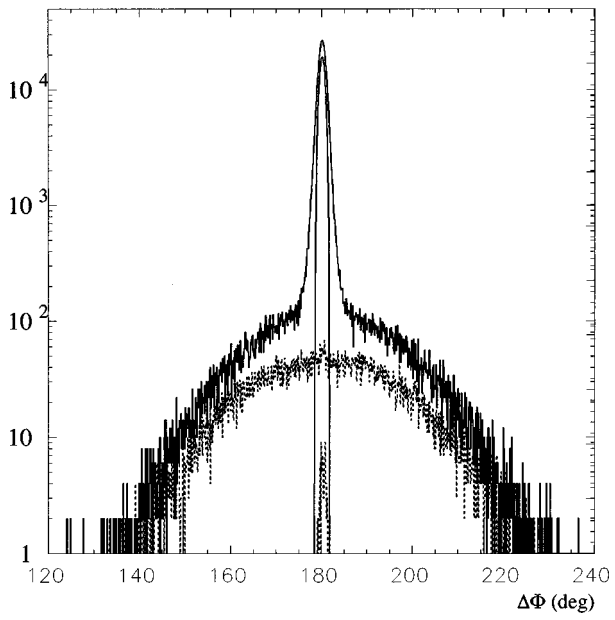

FIG. 13. Number of type II events vs difference in azimuthal angle between the two prongs. The spectrum with the H target shows a large narrow peak of (coplanar) pp events, superimposed on a broad peak of (nearly coplanar) background events. The lower curve is the spectrum with the N_2 target (dashed line). The sharp peaks represent the events that pass the cut imposed by the kinematic fit (Sec. III C 3).

background as a function of scattering angle. The effect of the background on the final data was estimated from a simulation with and without added background to the simulated yield. It was assumed that $A_y = 0$ for the background, which is a pessimistic assumption since the actual analyzing power for the quasifree pp peak of N is nearly the same as for pp elastic scattering. At all angles, the effect of background on the final data is less than 1/3 of the statistical error.

B. Absolute angle scale

The scattering angles determined by the kinematic fit have an uncertainty of $\leqslant 0.08°$ (Sec. III D 1). The angle scale can be checked from the measured $A_y(\theta)$ and $A_{xz}(\theta)$, since both quantities must cross zero at $\theta_{cm} = 90°$, i.e., $\theta_{lab} = \arctan[\sqrt{2/(1+\gamma)}] = 43.57°$, where γ is the relativistic γ factor. The weighted mean of the two zero crossings of 43.53 $\pm 0.10°$ is consistent with the expected value.

C. Polarization scale factor uncertainty

The angular distributions of the four polarization observables reported here are subject to an overall scale factor uncertainty arising from two independent influences: the uncertainty in the comparison to the reference data [1] and the scale factor uncertainty of the reference data themselves. The uncertainty arising from the comparison to the reference data was determined by repeating the normalization process described in Sec. VI B, each time changing one of the measured yields randomly by a Gaussian of width equal to the square root of the number of counts. From the spread of the resulting distribution in P and P^2 the probable errors of the normalization uncertainties were found to be $\delta P/P = 0.29\%$ and $\delta(P^2)/P^2 = 0.55\%$. Combined with the uncertainty of the reference data, the overall scale factor uncertainty is $\pm 1.3\%$ for the present $A_y(\theta)$ and $\pm 2.5\%$ for the $A_{mn}(\theta)$.

IX. RESULTS

The results are shown in Table III. Data at the smallest two angles are based on type Ib events, i.e., determination of the scattering angle from the recoil energy rather than from wire chamber information. Data between $\theta_{lab} = 5°$ and 12° can be processed either as type Ia or type Ib events, depending on whether the scattering angle is taken from wire-chamber information of the forward track or from the recoil energy. The two methods give consistent results. Analysis as type Ib event has the advantage that the analysis is constrained by the available information on wire chamber coordinates as well as information about the recoil energy. On the other hand, below 8° the forward proton passes through the hub of the wire chamber and thus is subject to multiple scattering of up to $\pm 0.2°$ (rms). For θ_{lab} from 5° to 7° the choice was to take the average of the values obtained by the two methods, but retain the larger of the statistical errors.

In the region between $\theta_{lab} = 30-35°$ a given event can be analyzed as type Ia or type II. The choice is made to analyze those events as type II, because the coplanarity condition of the two proton tracks yields more information about the event. While type II events include events with laboratory scattering angles up to $\theta_{lab} = 60°$, the table of results always

TABLE III. Analyzing power A_y and spin correlation coefficients A_{mn} at 197.4 MeV. In addition to the statistical uncertainties shown, the results are subject to a scale factor uncertainty of $\pm 1.3\%$ for A_y and $\pm 2.5\%$ for A_{mn}.

$\theta_{\rm lab}$ (deg)	A_y	A_{xx}	A_{yy}	A_{xz}
3.5	0.024±0.046	−0.204±0.164	0.134±0.164	−0.039±0.156
4.5	0.075±0.015	−0.128±0.054	0.027±0.054	−0.070±0.053
5.5	0.170±0.009	−0.460±0.031	−0.146±0.031	−0.068±0.031
6.5	0.196±0.006	−0.539±0.022	−0.204±0.022	−0.129±0.022
7.5	0.219±0.006	−0.579±0.020	−0.184±0.020	−0.206±0.019
8.5	0.229±0.005	−0.541±0.018	−0.146±0.018	−0.234±0.018
9.5	0.245±0.005	−0.538±0.017	−0.089±0.017	−0.259±0.016
10.5	0.252±0.004	−0.482±0.016	−0.016±0.016	−0.336±0.015
11.5	0.273±0.004	−0.439±0.015	0.106±0.015	−0.351±0.014
12.5	0.272±0.004	−0.475±0.014	0.193±0.014	−0.423±0.014
13.5	0.288±0.004	−0.433±0.014	0.262±0.014	−0.443±0.013
14.5	0.293±0.004	−0.421±0.013	0.311±0.013	−0.478±0.013
15.5	0.304±0.004	−0.427±0.013	0.419±0.013	−0.520±0.013
16.5	0.300±0.004	−0.445±0.013	0.482±0.013	−0.512±0.012
17.5	0.303±0.004	−0.456±0.012	0.548±0.012	−0.537±0.012
18.5	0.305±0.004	−0.502±0.012	0.596±0.012	−0.542±0.012
19.5	0.299±0.004	−0.517±0.012	0.660±0.012	−0.547±0.012
20.5	0.303±0.004	−0.528±0.013	0.725±0.013	−0.557±0.012
21.5	0.296±0.004	−0.571±0.013	0.727±0.013	−0.540±0.013
22.5	0.296±0.004	−0.592±0.013	0.826±0.013	−0.536±0.013
23.5	0.282±0.004	−0.612±0.014	0.853±0.014	−0.525±0.013
24.5	0.273±0.004	−0.632±0.014	0.860±0.014	−0.503±0.014
25.5	0.270±0.004	−0.668±0.015	0.877±0.015	−0.496±0.015
26.5	0.254±0.004	−0.696±0.016	0.874±0.016	−0.492±0.015
27.5	0.241±0.005	−0.741±0.016	0.892±0.016	−0.438±0.016
28.5	0.241±0.005	−0.729±0.017	0.909±0.017	−0.457±0.017
29.5	0.229±0.005	−0.772±0.018	0.955±0.018	−0.442±0.018
30.5	0.223±0.005	−0.793±0.019	0.970±0.019	−0.392±0.018
31.5	0.193±0.005	−0.831±0.018	0.944±0.018	−0.340±0.018
32.5	0.179±0.005	−0.849±0.017	0.954±0.017	−0.297±0.016
33.5	0.175±0.005	−0.852±0.016	0.974±0.016	−0.290±0.015
34.5	0.148±0.004	−0.873±0.015	0.949±0.015	−0.263±0.015
35.5	0.132±0.004	−0.892±0.014	0.951±0.014	−0.213±0.014
36.5	0.118±0.004	−0.895±0.013	0.976±0.013	−0.203±0.013
37.5	0.108±0.004	−0.915±0.013	0.964±0.013	−0.164±0.012
38.5	0.083±0.003	−0.908±0.012	0.973±0.012	−0.148±0.012
39.5	0.078±0.003	−0.911±0.011	0.959±0.011	−0.124±0.011
40.5	0.052±0.003	−0.917±0.011	0.956±0.011	−0.093±0.011
41.5	0.034±0.003	−0.918±0.011	0.973±0.011	−0.045±0.010
42.5	0.011±0.003	−0.929±0.010	0.953±0.010	−0.023±0.010
43.5	0.005±0.004	−0.948±0.014	0.942±0.014	0.021±0.013

lists the smaller of the laboratory angles of the two coincident protons.

The only previous spin correlation data at energies between 150 MeV and 300 MeV are the measurements of Ref. [1], which are more limited in angular range but have somewhat smaller statistical errors. The two data sets are independent except for one overall normalization constant (see Sec. VI B). Comparison of the four observables at 14 angles shows excellent agreement. The overall χ^2 is 43 for 55 degrees of freedom. The largest deviation occurs for A_y at the smallest angle common to both data sets (4.5°), where $\chi^2 = 10$ is large but not inconsistent with expectation for one datum out of 56.

The results are plotted in Fig. 14, which also shows a comparison to the phase shift analysis NI93 [17]. In this and the other graphs which follow, the data are plotted in 2° intervals for clarity. For this purpose the data for two adjacent 1° bins were added and the finite-bin correction (see Sec. VII C) was reevaluated to give the appropriate results at the center of the 2° bins.

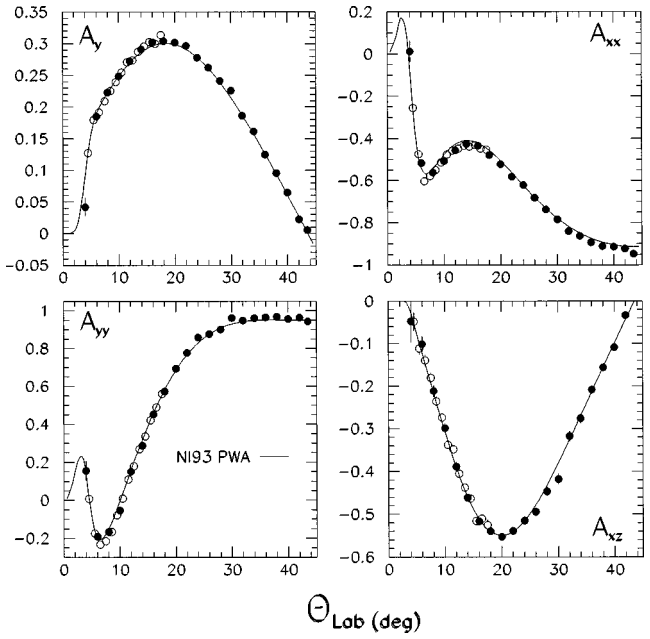

FIG. 14. A_y and A_{mn} vs angle (●). The data from Ref. [1] are also shown (○). The solid line corresponds to the recent NI93 partial wave analysis from Ref. [17].

X. COMPARISON TO THEORY

In the following we compare our results with current pp partial-wave analyses and with some recent nucleon-nucleon potential models. The analysis of the previous forward-angle data reported in [1] will be updated by including the most recent calculations.

One difficulty encountered in the comparison to theory is that the accuracy of the experiments has reached a stage where rather small differences in the calculations become significant. We note, for instance, that comparison of the present data for the Argonne potential [18] gave a different result ($\chi^2=1.5$ vs 2.0), depending on whether one uses calculations provided by Stoks [19] or by the SAID interactive program [14]. Similar differences were found in other cases. The differences are most likely caused by different assumptions, e.g., about electromagnetic effects. It seemed thus most appropriate to quote calculated values obtained directly from the respective theory group that carried out the original analysis.

All comparisons to partial-wave analyses (PWA) use energy-dependent PWA analyses in which all NN elastic scattering data over a range of energies are fitted with parametrized energy dependences of the phase parameters. The particular solutions used here are the following.

SM94: an analysis of 12838 pp and 10918 np data points in the energy range 1–1600 MeV, published by the Virginia group in 1994 [20]. Numerical values reported here have been obtained from the SAID interactive program. For the pp data set, χ^2 per datum is 22371/12838=1.74.

VZ40: same data base and same analysis as above, but restricted to the energy range 0–400 MeV (2170 pp and 3367 np data). For the pp data set the χ^2 per datum is 1.43.

WI96: represents the improvement of SM94 during the following three years. Numerical values, obtained from the SAID interactive program [14], reflect the status of the analysis of December 1996. In contrast to SM94, the data for this analysis contain the analyzing power and spin correlation parameters at 197 MeV which have been measured previously by our group [1].

SM97: the most recently published analysis of NN elastic scattering by the Virginia group [21]. The parametrization is the same as for SM94, but the new analysis for pp extends to energies up to 2500 MeV and includes a substantial amount of new data above 500 MeV. Below 500 MeV, the only significant new data are the analyzing powers and spin correlation parameters at 197 MeV of Ref. [1].

NI93: the published PWA of the Nijmegen group [17], covering the energy range 0–350 MeV. Numerical values reported here were obtained from Ref. [22]. For the 1787 pp data, the χ^2/DOF is 1.08.

NI97: the numerical results of this yet unpublished update of NI93 were obtained from Ref. [22]. In contrast to NI93, the data base contains the analyzing powers and spin correlation parameters at 197 MeV which have been measured previously by our group [1].

A comparison of these calculations with the data of Table III is presented in Table IV. The χ^2 summed over the 41 data points of the angular distribution is given for each observable. Also shown is the χ^2 for all observables combined and the χ^2 per degree of freedom. In comparing to the calculations we take into account that the measurements have an overall normalization uncertainty. Thus in each case the measured values were multiplied by normalization factors κ and κ^2 for A_y and A_{mn}, respectively, until best agreement with the calculation is reached. The scale factor for A_{mn} is the square of the scale factor for A_y, because the A_{mn} involve beam and target polarization. In all cases the required κ is well within the range of the normalization error discussed in Sec. VIII C.

Comparison between data and calculations are further illustrated in Fig. 15. To make small differences more visible, reference values $A^{\rm ref}$ were subtracted from data and calculations. Here we chose the NI93 solution as a reference, but it should be clear that the choice of reference is quite arbitrary.

Inspection of Table IV and Fig. 15 shows that the NI93 analysis, which preceded the present measurements, agrees well with the data. Although the overall χ^2 for the world data is very good (χ^2/DOF=1.08) there are systematic deviations from the present measurements. Since this solution is chosen as the reference in Fig. 15, ideally the points would lie on the zero line, but one notes that both A_{xx} and A_{yy} are below the calculation forward of 20°. However, the agreement with the present measurements is much better than for the earlier data [1]. The recent Nijmegen analysis NI97, which includes the previous data [1] in the fit, gives even better agreement as indicated by the dotted line in Fig. 15 and the even better χ^2 (Table IV).

The progress in the VPI solution over the past four years has been pronounced, going from large systematic deviations for SM94 (solid line in Fig. 15, χ^2/DOF=5.28) to the much improved solution SM97 (dashed line in Fig. 15, χ^2/DOF =2.11) with WI96 intermediate between these two. It is not clear why A_{xx} improved much less than the other three observables. Most of the improvement seen in SM97 is already present in the earlier WI96, a solution which already incorporated the earlier forward angle A_y, A_{mn} by our group, but

TABLE IV. Comparison between the data of Table III and different partial-wave and potential-model analyses. An overall scale factor κ for A_y and κ^2 for A_{mn} was allowed for best normalization to the theoretical A_y and A_{mn}. The χ^2 summed over the 41 data points of the angular distribution is given for each observable. Also given is the sum of the χ^2 for all observables and the overall χ^2 per degree of freedom (DOF).

Type of analysis		Ref.	κ	χ^2 (41 angles) A_y	A_{xx}	A_{yy}	A_{xz}	Sum	χ^2/DOF
SM94		[20]	0.9997	252.2	234.0	67.4	322.7	866.3	5.28
WI96	Partial	[14]	1.0006	65.1	129.4	63.2	201.9	459.6	2.80
SM97	wave	[21]	0.9927	74.6	150.8	52.7	67.3	345.4	2.11
VZ40	analysis	[20]	0.9963	69.9	202.7	133.3	66.0	471.9	2.88
NI93 PWA		[17]	0.9931	63.8	53.7	80.6	38.3	236.4	1.44
NI97 PWA		[22]	0.9916	66.6	45.1	53.4	34.2	199.3	1.22
AV18		[18]	0.9917	67.4	73.6	67.6	44.2	252.9	1.54
CD-BONN		[26]	0.9913	84.9	54.0	54.0	40.7	233.6	1.42
PARIS	Potential	[24]	0.9903	102.2	254.0	127.1	268.0	751.2	4.58
NJM I	models	[25]	0.9917	63.1	45.2	52.3	34.2	194.8	1.19
NJM93		[25]	0.9936	150.4	110.8	113.5	78.6	453.3	2.76
OSBEP		[27]	0.9928	271.1	179.4	357.2	65.0	872.7	5.32
REID93		[25]	0.935	62.5	56.5	66.8	35.7	221.4	1.35

not the new, accurate cross section data from EDDA above 500 MeV [23]. The small improvement in our χ^2 for SM97 compared to WI96 is then presumably due to the improved energy dependence obtained by the addition of new data above 500 MeV.

Nuclear structure calculations require the description of the *NN* interaction in terms of a potential. Table IV and Fig. 16 show comparison of the present data with several recent potential models, as well as the historic Paris potential [24]. The following potentials are included in the comparison.

AV18: The most recent Argonne potential uses a phenomenological form at short distances [18]. The charge-dependent potential has been fit directly to the Nijmegen PWA and to the deuteron binding energy.

NJM93: The Nijmegen soft core potential. A conventional meson-exchange potential described in Ref. [25].

NJM I: A nonlocal potential based on NJM93, in which the potential for each partial wave is adjusted phenomenologically [25]. The quality of fit to the *NN* data is almost equal to the Nijmegen PWA.

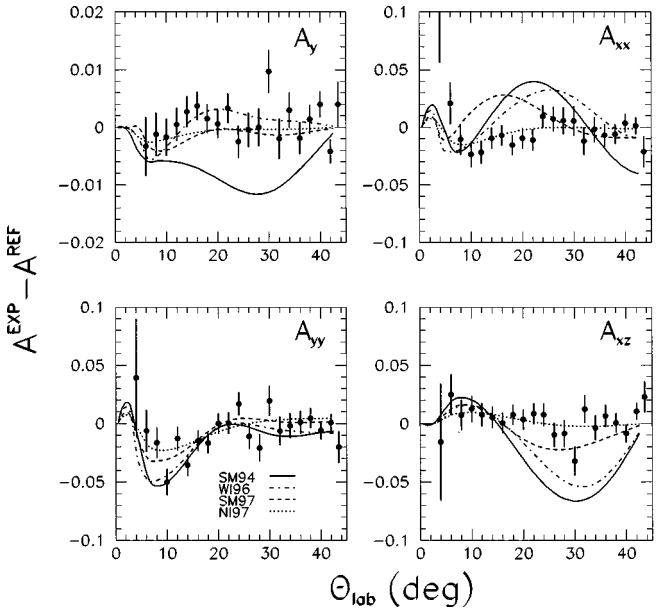

FIG. 15. Comparison between data and different partial wave analyses of the *pp* interaction. In order to display small differences more clearly, reference values A^{ref}, calculated from the NI93 PWA (see Ref. [17]), are subtracted. For other references to the calculated curves, see Table IV.

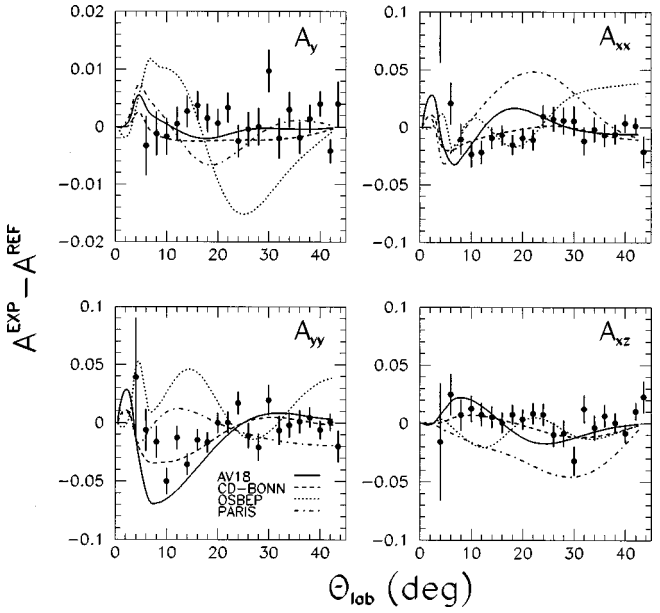

FIG. 16. Comparison between data and different potential models of the *pp* interaction. In order to display small differences more clearly, reference values A^{ref}, calculated from the NI93 PWA (see Ref. [17]), are subtracted. For other references to the calculated curves, see Table IV.

REID93: A nonlocal, Reid-like potential constructed by the Nijmegen group, which gives as good a fit to the pp data set as the Nijmegen partial-wave analysis [25].

CD-BONN: The charge-dependent version of the Bonn potential [26]. Small adjustments were allowed in each partial wave for the parameters that govern the correlated multipion exchange. Numerical values for comparison to the data were obtained from the SAID interactive program [14].

OSBEP: The ''One Solitary Boson Exchange Potential,'' developed recently by the Hamburg group [27], is based on a nonlinear model of self-interacting mesons as a substitute for the commonly used phenomenological form factors. This significantly reduces the number of parameters in the boson exchange potential (8 parameters in OSBEP vs 15 in NJM93). While Ref. [27] reports that the OSBEP predictions were consistent with our previous forward angle measurements of A_y [1], the present A_y and A_{yy} are not well reproduced by this calculation over a wider range of angles.

In Fig. 16, some of the above potential model results are shown, using again as the reference A^{ref} the Nijmegen PWA NI93. The progress from the classic Paris potential (dash-dotted line) to the new CD-Bonn nonlocal, charge-dependent potential (dashed line) is clearly seen in Fig. 16 and the improved χ^2 (Table IV). The agreement obtained with the new OSBEP potential is not nearly as good as for CD-BONN or REID93, but in contrast to OSBEP, the latter potentials sacrifice the simplicity of the original boson-exchange potentials and fit each partial wave separately.

XI. CONCLUSIONS

We report the results from the second experiment with an internal polarized gas target in the Indiana proton storage ring (''Cooler''). The present measurements of analyzing power A_y and spin correlation parameters A_{xx}, A_{yy}, and A_{xz} at 197.4 MeV extend the earlier forward-angle measurements to the full angular range of $\theta_{\mathrm{c.m.}}=7°-90°$. The scattering angle was determined by track reconstruction (kinematic fitting) of information provided by wire chambers and silicon-strip recoil detectors. Results, reported here in 1° bins, have statistical errors of <0.02 for the A_{mn} and about 0.005 for A_y. Except for the data in Ref. [1] none of the spin correlation coefficients has previously been measured in the energy range 150 MeV to 300 MeV. The present results confirm the prediction of very large spin-spin effects in the pp interaction, with A_{yy} reaching values as high as 0.96 near $\theta_{\mathrm{c.m.}}=90°$.

Since the world set of pp data comprises some 10 000 data points below 1000 MeV and roughly 2000 points below 350 MeV, one may wonder if additional experimental and theoretical work on pp elastic scattering at this point has any impact at all. However, the comparison of the present results to theory illustrate that significant progress has been made during the past four years. The 1993 Nijmegen partial-wave analysis [17], which is limited to energies below 350 MeV, gives excellent agreement to the world data set in this energy range. Comparison to the new data again shows good overall agreement but exhibits small systematic deviations from the measured A_{xx} and A_{yy} for angles forward of $\theta_{\mathrm{lab}}=20°$. These particular deviations are much reduced by a new Nijmegen phase shift analysis, which included in its data base our previous measurements at forward angles. The 1994 phase shift analysis for the energy range 1–1600 MeV by the VPI group gives a much less satisfactory representation of the present results. However, the past four years have led to a very large improvement. The new analysis includes in the data base our previous forward angle spin correlation measurements as well as excellent new cross section data and various spin observables above 500 MeV. The overall quality of fit for the new solution is much improved over the old one, both for the world data set and for the limited data presented here, but compared to our measurements significant systematic deviations suggest the need for further refinements. Among the potential models the Reid-like potential by the Nijmegen group stands out for the high quality of agreement with all data below 350 MeV, including the present new measurements. For the present data, the CD-Bonn and the Argonne AV18 potential give equally satisfactory representations.

On the experimental side, the present measurements again showed the viability of the new technique based on internal polarized gas targets in a storage ring with electron cooling of the circulating polarized beam. Data acquisition rate was improved by a new mode of operation, where the spin of the beam in the ring was reversed with a spin-flipper, so that the existing beam could be retained in the ring when beam of opposite polarization was injected. This mode increased the average luminosity by about a factor 4. The other new feature in this experiment was that during part of each cycle the beam was accelerated and then again decelerated to the original energy. This allowed new measurements to be made for energies between 250 and 450 MeV, and has allowed accurate polarization calibration for this energy range. As far as the present results are concerned, interleaving the 197.4 MeV measurements with the runs at higher energies was only a disadvantage, since this mode, in the presence of the restrictive acceptance of the target cell, made tuning of the accelerator very challenging. On the other hand, the experience that a storage ring can be ramped up and down in the presence of a polarized target cell represented an interesting advance in the study of spin-spin phenomena. A report on our spin correlation results for seven energies between 250 MeV and 450 MeV is in preparation. No doubt, applications of our methods to pp experiments at the COSY ring, with beam energies up to 2.5 GeV, will yield a wealth of new spin-spin data in the near future.

ACKNOWLEDGMENTS

We thank Dr. J. J. deSwart, Dr. M. C. M. Rentmeester, and Dr. V. G. J. Stoks for providing tables of numerical results for comparison to the present data, and for permission to include results from their as yet unpublished new phase shift analysis. We are grateful for the untiring efforts of the accelerator operations group at IUCF, in particular G. East and T. Sloan. This work was supported in part by the National Science Foundation and the Department of Energy. One of us (F.R.) would also like to thank the Alexander von Humboldt Foundation for their generous support.

[1] W. Haeberli, B. Lorentz, F. Rathmann, M. A. Ross, T. Wise, W. A. Dezarn, J. Doskow, J. G. Hardie, H. O. Meyer, R. E. Pollock, B. von Przewoski, T. Rinckel, E. Sperisen, and P. V. Pancella, Phys. Rev. C **55**, 597 (1997).
[2] R. E. Pollock, Annu. Rev. Nucl. Part. Sci. **41**, 357 (1991).
[3] T. Wise, A. D. Roberts, and W. Haeberli, Nucl. Instrum. Methods Phys. Res. A **336**, 410 (1993).
[4] W. Haeberli, Annu. Rev. Nucl. Sci. **17**, 373 (1967).
[5] M. A. Ross, W. K. Pitts, W. Haeberli, H. O. Meyer, P. V. Pancella, S. F. Pate, R. E. Pollock, B. von Przewoski, T. Rinckel, J. Sowinski, and F. Sperisen, Nucl. Instrum. Methods Phys. Res. A **326**, 424 (1993).
[6] Type J Silicon Strip detectors, supplied by Micron Semiconductor Ltd., Lancing Sussex, England.
[7] H. O. Meyer, C. Horowitz, H. Nann, P. V. Pancella, S. F. Pate, R. E. Pollock, B. von Przewoski, T. Rinckel, M. A. Ross, and F. Sperisen, Nucl. Phys. **A539**, 633 (1992).
[8] K. Solberg, A. Eads, J. Goodwin, P. Pancella, H. O. Meyer, T. Rinckel, and M. A. Ross, Nucl. Instrum. Methods Phys. Res. A **281**, 283 (1989).
[9] B. von Przewoski, W. A. Dezarn, J. Doskow, J. G. Hardie, H. O. Meyer, R. E. Pollock, T. Rinckel, F. Sperisen, W. Haeberli, B. Lorentz, F. Rathmann, T. Wise, and P. V. Pancella, Rev. Sci. Instrum. **67**, 165 (1996).
[10] R. E. Pollock, Nucl. Phys. **A626**, 385c (1997).
[11] Review of Particle Properties, Phys. Rev. D **54**, 158 (1996).
[12] R. E. Pollock, W. A. Dezarn, M. Dzemidzic, J. Doskow, J. G. Hardie, H. O. Meyer, B. v. Przewoski, T. Rinckel, F. Sperisen, W. Haeberli, B. Lorentz, F. Rathmann, T. Wise, and P. V. Pancella, Phys. Rev. E **55**, 7606 (1997).
[13] H. O. Meyer, Phys. Rev. C **56**, 2074 (1997).
[14] The SAID dial-in. Available via TELNET to `clsaid-.phys.vt.edu`, with `userid:said` (no password required).
[15] G. G. Ohlsen, Rep. Prog. Phys. **35**, 717 (1972).
[16] J. Bystricky, F. Lehar, and P. Winternitz, J. Phys. (Paris) **39**, 1 (1978).
[17] V. J. G. Stoks, R. A. M. Klomp, M. C. M. Rentmeester, and J. J. deSwart, Phys. Rev. C **48**, 792 (1993).
[18] R. B. Wiringa, V. G. J. Stoks, and R. Schiavilla, Phys. Rev. C **51**, 38 (1995).
[19] V. G. J. Stoks, `vstoks@physics.adelaide.edu.au` (private communication).
[20] R. A. Arndt, I. I. Strakovsky, and R. L. Workman, Phys. Rev. C **50**, 2731 (1994).
[21] R. A. Arndt, C. H. Oh, I. I. Strakovsky, R. L. Workman, and Frank Dohrmann, Phys. Rev. C **56**, 3005 (1997).
[22] J. J. deSwart and M. C. M. Rentmeester, Katholicke Universiteit Nijmegen (private communication).
[23] EDDA Collaboration, D. Albers, J. Bisplinghoff, R. Bollmann, K. Küßer, P. Cloth, R. Daniel, O. Diehl, F. Dohrmann, H. P. Engelhardt, J. Ernst, P. D. Eversheim, M. Gasthuber, R. Gebel, J. Greiff, A. Gross, R. Gross-Hardt, S. Heider, A. Heine, F. Hinterberger, M. Igelbrink, R. Jahn, M. Jeske, U. Lahr, R. Langkau, J. Lindlein, R. Maier, R. Maschuw, T. Mayer-Kuckuk, F. Mosel, M. Müller, M. Münstermann, D. Prasuhn, H. Rohdjess, D. Rosendaal, U. Ross, P. von Rossen, H. Scheid, N. Schirm, M. Schulz-Rojahn, F. Schwandt, V. Schwarz, W. Scobel, G. Sterzenbach, H. J. Trelle, A. Wellinghausen, W. Wiedmann, K. Woller, and R. Ziegler, Phys. Rev. Lett. **78**, 1652 (1997).
[24] M. Lacombe, B. Loiseau, J. M. Richard, R. Vinh Mau, J. Côté, P. Pirès, and R. de Tourreil, Phys. Rev. C **21**, 861 (1980).
[25] V. G. J. Stoks, R. A. M. Klomp, C. P. F. Terheggen, and J. J. deSwart, Phys. Rev. C **49**, 2950 (1994).
[26] R. Machleidt, F. Sammarruca, and Y. Song, Phys. Rev. C **53**, 1483 (1996).
[27] L. Jäde and H. V. von Geramb, Phys. Rev. C **57**, 496 (1998).